Quasi-Ray Gaussian Beam Algorithm for Short-Pulse Two-Dimensional Scattering by Moderately Rough Dielectric Interfaces

Vincenzo Galdi, *Member, IEEE,* Leopold B. Felsen, *Life Fellow, IEEE,* and David A. Castañon, *Senior Member, IEEE*

***Abstract*—We consider short-pulse (SP) time-domain (TD) two-dimensional (2-D) scattering by moderately rough interfaces, which separate free space from a slightly lossy dielectric half-space, and are excited by one–dimensional (1-D) SP-TD aperture field distributions. This study extends to the SP-TD in our previous investigation of time-harmonic *high frequency* 2-D scattering of Gabor-based quasi-ray Gaussian beam fields excited by 1-D aperture field distributions in the presence of moderately rough dielectric interfaces (Galdi *et al.*). The proposed approach is based on the Kirchhoff Physical Optics (PO) approximation in conjunction with the Gabor-based quasi-ray narrow-waisted Gaussian pulsed-beam (PB) discretization (Galdi *et al.*), which is applied to the SP-induced equivalent magnetic surface currents on the interface that establish the TD reflected/transmitted fields. We show that, for well-collimated truncated SP incident fields, the PO-PB synthesis of the reflected/transmitted fields yields an approximate *explicit* physically appealing, numerically efficient asymptotic algorithm, with well-defined domains of validity based on the problem parameters. An extensive series of numerical experiments verifies the accuracy of our method by comparison with a rigorously-based numerical reference solution, and assesses its computational utility. The algorithm is intended for use as a rapid forward solver in SP-TD inverse scattering and imaging scenarios in the presence of moderately rough dielectric interfaces.**

***Index Terms*—Gaussian beams (GBs), rough surface scattering, short pulses.**

I. Introduction

THIS PAPER is concerned with the short-pulse (SP) time-domain (TD) scattering of two-dimensional (2-D) fields by one-dimensional (1-D) moderately rough-dielectric interfaces, which separate free space from a slightly lossy dielectric half-space, and are excited by well-collimated incident fields from SP planar 1-D truncated aperture distributions. Restricting the analysis to the high-frequency range, a physical optics (PO) approach [3] is used to compute the TD reflected and transmitted fields. Specifically, an E formulation of PO is used [3], which is based on an equivalent magnetic surface current (EMSC), and renders the reflection and transmission problem equivalent to radiation from a locally varying time-delayed SP aperture field distribution along the interface profile. This SP-PO EMSC distribution is parameterized in terms of Gabor-based narrow-waisted ray-like discretized Gaussian initial fields on the interface, which generate reflected/transmitted pulsed beam (PB) propagators. The field at the observer in either half-space is established by summation over the SP-PO basis beams.

The problem strategy outlined above implements a further step in our planned sequential approach toward a robust physically incisive, accurate, and numerically efficient high-frequency asymptotic algorithm that quantifies SP scattering of three-dimensional (3-D) vector fields by 2-D moderately rough interface profiles between free space and slightly lossy-dielectric media. The intended application is as a rapid forward solver in SP-TD inverse scattering and imaging scenarios where a dielectric rough interface plays a critical role [our approach differs from several numerical/statistical approaches that have been explored in the past (see, e.g., [4]–[6] and the references therein)]. The general problem of SP-TD fields excited by 1-D planar-aperture distributions parameterized in terms of SP Gaussian beams (GBs) has already been addressed in one of our previous investigations [2]. The new step in the present problem is the inversion to the SP-TD of the scattered fields, in our previous study that deals with the same complete 2-D problem geometry, but is excited by time-harmonic high-frequency illumination; here the discretized Gabor basis for the 1-D planar truncated aperture distribution involves ray-like frequency domain GB propagators [1]. The coordination of [2] with the SP-TD inversion of the reflected/transmitted fields in [1] occupies the remainder of this paper. After the problem statement in Section II, we reexamine in Section III the high-frequency solution in [1], and modify it by introducing the PO approximation for the induced surface fields on the interface in order to facilitate *explicit* analytic inversion to the SP-TD later on; the corresponding PO-modified asymptotic GB propagators excited by illumination from a quasi-linearly phased, truncated-aperture distribution are developed here. The inversion to the SP-TD is treated in Section IV, with preliminary frequency-domain approximations for slightly-lossy

Manuscript received April 5, 2001; revised November 30, 2001. This work was supported in part by ODDR&E under MURI Grants ARO DAAG55-97-1-0013 and AFOSR F49620-96-1-0028, and by the Engineering Research Centers Program of the National Science Foundation under Award EEC-9986821. The work of V. Galdi was also supported by a European Union Postdoctoral Fellowship through the University of Sannio, Benevento, Italy. The work of L. B. Felsen was also supported in part by the U.S.-Israel Binational Science Foundation, under Grant 9900448, and by the Polytechnic University, Brooklyn, NY.

V. Galdi was with the Department of Electrical and Computer Engineering, Boston University, Boston, MA 02215 USA, and is now with the University of Sannio, Benevento, Italy (e-mail: vgaldi@unisannio.it).

D. A. Castañon is with the Department of Electrical and Computer Engineering, Boston University, Boston, MA 02215 USA (e-mail: dac@bu.edu).

L. B. Felsen is with the Department of Aerospace and Mechanical Engineering and the Department of Electrical and Computer Engineering, Boston University, Boston, MA 02215 USA, and is also Professor Emeritus with the Polytechnic University, Brooklyn, NY 11201 USA (e-mail: lfelsen@bu.edu).

Digital Object Identifier 10.1109/TAP.2003.809102

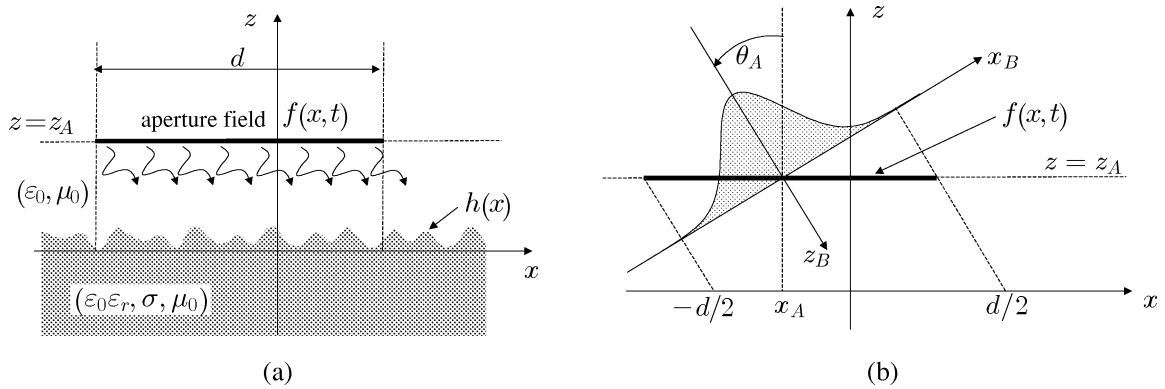

Fig. 1. (a) Problem geometry. An aperture-generated TM-polarized pulsed field impinges from free space onto a dielectric half-space with relative permittivity ϵ_r and conductivity σ, bounded by a moderately rough interface $z = h(x)$. (b) Wide-waisted Gaussian beam excitation in (2), to be approximated as in (3).

dielectrics as well as certain basis-beam parameters that adapt the inversion to the SP-TD aperture field parameterization in [2]. The numerical experiments in Section V, performed for a variety of different problem parameters, assess, and quantify the accuracy, range of validity, and computational utility of the algorithm in Section IV through comparisons with a rigorously-based numerical reference solution. Conclusions are briefly stated in Section VI.

II. Statement of the Problem

The problem geometry is sketched in Fig. 1. All fields and geometries are 2-D in the y independent (x, z) space. A transverse magnetic (TM) polarized pulsed electromagnetic (EM) field is assumed to impinge from free space onto a homogeneous, slightly lossy, dielectric half-space bounded by an irregular interface described by a continuous function $h(x)$ [Fig. 1(a)].

A. Incident Field

We restrict our attention to the y directed electric field $e(x, z, t)$ from which all other field quantities of interest can be computed via Maxwell's equations. The y directed incident field e^i is generated by a large truncated 1-D aperture of width d at $z = z_A$, with an assigned space–time electric field distribution $f(x, t)$,

$$e^i(x, z = z_A, t) = \begin{cases} f(x,t), & |x - x_A| \le \frac{d}{2} \\ 0, & |x - x_A| > \frac{d}{2} \end{cases} \tag{1}$$

where x_A is a spatial shift which can be used to adjust the illumination. In what follows, we shall be concerned with pulsed well-collimated Gaussian beams (GBs) generated by the separable linear-delay space–time field distributions

$$f(x,t) = g[(x - x_A)\cos\theta_A]p[t - c^{-1}(x - x_A)\sin\theta_A]. \tag{2}$$

In (2), $g(x)$ is a Gaussian taper function and $c = (\epsilon_0\mu_0)^{-1/2}$ is the free-space wavespeed, with ϵ_0, μ_0 denoting the free-space permittivity and permeability, respectively. Moreover, $p(t)$ is a short pulse of length $T \ll d/c$, and θ_A denotes the tilt angle of the radiated beam relative to the z axis [Fig. 1(b)]. The variance of $g(x)$ and the spatial shift x_A are chosen so that $f(x, t)$ tapers to zero for $|x| > d/2$, as shown in Fig. 1(b). The linear-delay aperture field distribution in (2) generates a *wide-waisted* tilted GB which, in the collimation zone of the aperture, can be approximated by a pulsed tapered plane wave

$$e^i(x, z, t) \sim g(x_B)p(t - c^{-1}z_B) \tag{3}$$

where (x_B, z_B) are beam centered coordinates [Fig. 1(b)]

$$\begin{bmatrix} x_B \\ z_B \end{bmatrix} = \begin{bmatrix} \cos\theta_A & \sin\theta_A \\ \sin\theta_A & -\cos\theta_A \end{bmatrix} \begin{bmatrix} x - x_A \\ z - z_A \end{bmatrix}. \tag{4}$$

The reference solutions employed later on are based on the incident field generated by numerical evaluation of the rigorous Kirchhoff aperture (line source Green's function) integration using (1) and (2) [with (10)], whereas all subsequent beam-derived results rely on the planewave approximation in (3).

B. Reflected and Transmitted Fields

The irradiated half-space is assumed to be nonmagnetic, i.e., with relative permeability $\mu_r = 1$ and characterized by the constant relative permittivity ϵ_r and electric conductivity σ, both being frequency independent. The interface profile is assumed to be *moderately* rough (both in height and slope) with respect to the pulse length T, i.e., the undulations in $h(x)$ are assumed to be on the order of cT. The reflected and transmitted fields are modeled via the Gabor-based narrow-waisted discretized pulsed beam (PB) algorithm in [2], to which we shall refer frequently throughout the paper.

III. Frequency-Domain Formulation

A Gabor-based, narrow-waisted GB approach for time-harmonic scattering by, and transmission through, moderately rough interfaces has been introduced in [1], extending the results in [7] and [8], and yielding a robust and efficient numerical algorithm. Although an extension of this approach to *pulsed* excitation, via analytic Fourier inversion, is possible in principle, its implementation is indirect and cumbersome. In particular, multiple interactions, which can be treated conveniently in the frequency domain (FD) (see [1, App. A]), would involve substantial preliminary algebra in the TD. Accordingly, we pursue here a simplified approach based on the FD Kirchhoff PO approximation which, via the algorithm in [2], can be more easily inverted to the TD. In this section,

we briefly review the FD PO formulation and its Gabor-based narrow-waisted beam discretization. Capital letters identify FD field quantities.

A. PO Approximation

The Kirchhoff PO approximation has been used extensively for scattering from smooth, gently-curved structures which are large on the wavelength scale [9]. Although, most applications have been carried out for impenetrable structures, penetrable objects can be handled as well (see, e.g., [3]). Applications to *conducting* rough surface scattering have also received much attention (see, e.g., [10]–[13]). For *penetrable* rough interfaces, we return to the geometry in Fig. 1(a), subject to the pulsed tapered plane-wave illumination in (3), with FD spectrum

$$E^i(x,z,\omega) \sim g(x_B)P(\omega)\exp(ik_0 z_B). \tag{5}$$

Here, (x_B, z_B) are the beam coordinates defined in (4), $k_0 = \omega/c = 2\pi/\lambda_0$ is the free-space wavenumber, λ_0 is the free-space wavelength, and $P(\omega)$ is the spectrum of the pulse $p(t)$

$$P(\omega) = \int_{-\infty}^{\infty} p(t)\exp(i\omega t)dt. \tag{6}$$

The y directed FD PO reflected field in the half-space $z > h(x)$ can be expressed as (E formulation [3])

$$E^r(x,z,\omega) \sim -\int_{C_{PO}} J^r_{PO}(x',\omega) \times \frac{\partial}{\partial\zeta} G_{2D}(x,z;x',h(x');k_0)d\ell' \tag{7}$$

where C_{PO} extends over the illuminated portion of the 1-D surface $z = h(x)$, $d\ell'$ is the incremental arc-length measured along the surface tangent

$$d\ell' = \left[1 + \left(\frac{dh}{dx}(x')\right)^2\right]^{1/2} dx'$$
$$\frac{dh}{dx}(x') \equiv \frac{dh}{dx}(x)\bigg|_{x'} \tag{8}$$

and $\partial/\partial\zeta$ denotes the normal derivative (Fig. 2)

$$\frac{\partial}{\partial\zeta} \equiv \left[1 + \left(\frac{dh}{dx}(x')\right)^2\right]^{-1/2} \left[\frac{\partial}{\partial z} - \frac{dh}{dx}(x')\frac{\partial}{\partial x}\right]. \tag{9}$$

As stated previously, the incident field tapering is chosen so that the illuminated portion of the interface, C_{PO}, is essentially confined to the interval $|x| \le d/2$ [see Fig. 1(b)]. In (7), G_{2D} is the FD line-source Green's function

$$G_{2D}(x,z;x',z';k) = \frac{i}{4}H_0^{(1)}(kR)$$
$$R = \sqrt{(x-x')^2 + (z-z')^2} \tag{10}$$

with $H_0^{(1)}(\cdot)$ denoting the zeroth-order Hankel function of the first kind. The PO EMSC density J^r_{PO} is given by twice the tangential reflected electric field at the interface, obtained from the canonical solution of infinite plane-wave scattering by a plane-dielectric boundary locally tangent to the rough surface profile (Fig. 2)

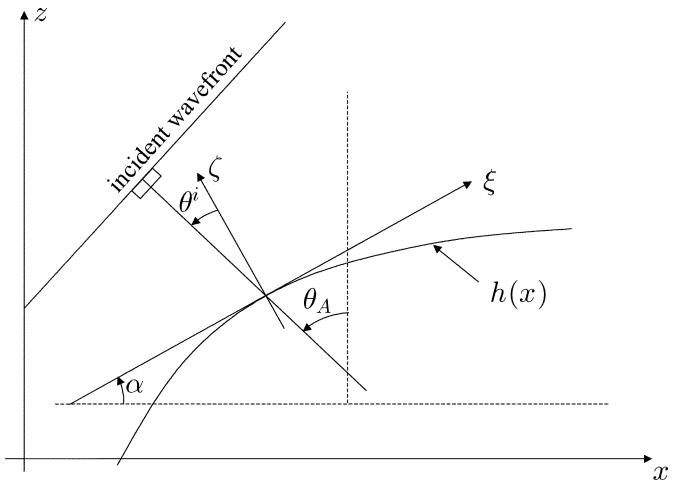

Fig. 2. Global (x,z) and local surface-based tangent-normal (ξ,ζ) coordinates. $\alpha(x) = \tan^{-1}[dh(x)/dx]$ is the local slope of the surface profile; $\theta^i(x) = \theta_A - \alpha(x)$ is the local incidence angle measured from the surface normal.

$$J^r_{PO}(x,\omega) = 2\mathcal{R}(x,\omega)E^i(x,h(x),\omega). \tag{11}$$

In (11), $\mathcal{R}$ denotes the local TM plane-wave Fresnel reflection coefficient

$$\mathcal{R}(x,\omega) = \frac{\cos\theta^i - \left(\epsilon_r^e - \sin^2\theta^i\right)^{1/2}}{\cos\theta^i + \left(\epsilon_r^e - \sin^2\theta^i\right)^{1/2}} \tag{12}$$

where

$$\epsilon_r^e(\omega) = \epsilon_r + i\frac{\sigma}{\omega\epsilon_0} \tag{13}$$

is the *effective* complex relative permittivity, and θ^i is the local incidence angle relative to the surface normal, which can be expressed in terms of the incident beam-tilt angle θ_A and the local slope α as (see Fig. 2)

$$\theta^i(x) = \theta_A - \alpha(x), \qquad \alpha(x) = \tan^{-1}\left[\frac{dh}{dx}(x)\right]. \tag{14}$$

The same considerations applied to the field transmitted into the half-space $z < h(x)$ yield

$$E^t(x,z,\omega) \sim \int_{C_{PO}} J^t_{PO}(x',\omega)\frac{\partial}{\partial\zeta}G_{2D}(x,z;x',h(x');k)d\ell' \tag{15}$$

where $k = \sqrt{\epsilon_r^e}k_0$ and the PO EMSC density J^t_{PO} is given by

$$J^t_{PO}(x,\omega) = 2[1 + \mathcal{R}(x,\omega)]E^i(x,h(x),\omega). \tag{16}$$

The limitations of the Kirchhoff PO approximation have been thoroughly investigated in the past and are well documented in the technical literature (for the case of conducting rough surface scattering see, e.g., [10]). In general, this approximation works well for large, smooth scatterers, and for observation directions not far from backscatter. The formulations in (7) and (15) neglect multiple interactions, which can be incorporated

in principle through higher order models (see, e.g., [13]). Here, we restrict the range of validity to moderate roughness (both in height and slope) and incidence directions far from grazing, thereby, avoiding multiple scattering. While the FD results in this Section are not restricted with respect to dielectric losses, our subsequent TD applications are subject to the "slight loss" assumption which is exploited in Section IV-A to symplify analytic inversion to the TD.

B. Gabor-Based Narrow-Waisted Gaussian Beam Discretization

The FD PO integrals in (7) and (15) are formally analogous to the FD Kirchhoff aperture radiation integrals in [2, Sec. II], [2, eq. (2)]. The only difference is that the line integration in (7) and (15) is performed along the 1-D rough surface profile $z = h(x)$ instead of a 1-D planar aperture as in [2, Sec. II]. In [2], the assigned FD planar aperture field distribution is parameterized in terms of x domain discretized m indexed Gabor basis functions with narrow width L, centered on the Gabor lattice points $x_m = mL$ on the aperture; these initial conditions generate *narrow-waisted*, quasi-ray GBs, which can be approximated efficiently in terms of *complex source point* (CSP) propagators (see [2, eq. (14)]). *Nontilted* beams, launched from the Gabor lattice points and propagating along the direction *normal* to the aperture plane, are superposed to synthesize the radiated field (see [2, eq. (13)]), with the Gabor coefficients approximated efficiently by *sampling* the aperture field distribution (see [2, eq. (12)]). All other *tilted* beams in the full Gabor GB expansion [2, eq. (8)], which are evanescent for $L \lesssim \lambda_0 \ll d$, are neglected. For linearly phased apertures (cf. [2, eq. (17)]), a more efficient parameterization is obtained by exploiting propagation-matched tilted beams (cf. [18, eqs. (18)–(22)]). For *plane* dielectric interfaces, the plane-wave-excited PO EMSC would be *exactly* linearly phased; and therefore, the tilted beam discretization in [2, eqs. (18)–(22)] could be applied straightforwardly and as shown in [2, Sec. II-C], would be considerably more efficient than the nontilted beam algorithm in [2, eqs. (13)–(16)]. For *moderately rough* interfaces, the phasing in the PO EMSC is no longer *globally* linear. However, for narrow-waisted beams, one can still exploit the *locally* linear behavior. To this end, it is expedient to rewrite the PO EMSC by separating out the locally linear-phase term that the incident plane wave would induce on the locally tangent plane, i.e., generalizing [2, eq. (17)]

$$J^{\nu}_{PO}(x) = \mathcal{J}^{\nu}_{PO}(x) \exp\left[\frac{ik_0 x \sin\theta^i(x)}{\cos\alpha(x)}\right], \qquad \nu = r \text{ or } t \tag{17}$$

with $\theta^i(x)$ and $\alpha(x)$ defined in (14). Here and henceforth, the ω dependence is omitted for simplicity of notation. The weakly phased *reduced* PO EMSC

$$\mathcal{J}^{\nu}_{PO}(x) = J^{\nu}_{PO}(x) \exp\left[\frac{-ik_0 x \sin\theta^i(x)}{\cos\alpha(x)}\right], \qquad r = r \text{ or } t \tag{18}$$

can thus be parameterized approximately as (cf. [2, eqs. (18–19)])

$$\mathcal{J}^{\nu}_{PO}(x) \approx \sum_{|m| \le (d/2L)} C^{\nu}_m w(x - x_m), \quad x_m = mL; \quad \nu = r \text{ or } t \tag{19}$$

where the subscript $_m$ tags the mth GB in the discretization and $w(\cdot)$ represents the normalized Gaussian window in [2, eq. (6)]

$$w(x) = \left(\frac{\sqrt{2}}{L}\right)^{1/2} \exp\left[-\pi\left(\frac{x}{L}\right)^2\right], \qquad \int_{-\infty}^{\infty} w^2(x)dx = 1 \tag{20}$$

with the Gabor coefficients C^{ν}_m given approximately by

$$C^{\nu}_m = \left(\frac{L}{\sqrt{2}}\right)^{1/2} \mathcal{J}^{\nu}_{PO}(x_m), \qquad \nu = r \text{ or } t. \tag{21}$$

The sum in (19) extends up to $|m| \le d/2L$ because the PO EMSC (subject to verification) are assumed to be negligible for $|x| \ge d/2$, outside the illumination window [see Fig. 1(b)]. By combining (7) and (15) with (17) and (19), the reflected and transmitted fields can be discretized as (see also [2, eq. (18)])

$$E^{\nu}(x,z) \sim \frac{1}{2} \sum_{|m| \le (d/2L)} C^{\nu}_m \mathcal{B}^{\nu}_m(x,z), \qquad \nu = r \text{ or } t \tag{22}$$

where the beam propagators $\mathcal{B}^r_m$, $\mathcal{B}^t_m$ are given by

$$\mathcal{B}^r_m(x,z) = -2\int_{C_{PO}} w(x' - x_m) \times \frac{\partial}{\partial\zeta} G_{2D}(x,z;x',h(x');k_0) \times \exp\left[\frac{ik_0 x' \sin\theta^i(x')}{\cos\alpha(x')}\right] d\ell' \tag{23}$$

$$\mathcal{B}^t_m(x,z) = 2\int_{C_{PO}} w(x' - x_m) \times \frac{\partial}{\partial\zeta} G_{2D}(x,z;x',h(x');k) \times \exp\left[\frac{ik_0 x' \sin\theta^i(x')}{\cos\alpha(x')}\right] d\ell'. \tag{24}$$

For narrow Gaussian windows, i.e., $L \lesssim \lambda_0 \ll d$, and moderate surface roughness, the paraxial far zone approximation in [7] can be applied to (23) and (24). For the reflected field, one obtains the following *complex source point* (CSP) approximation which applies [2, eq. (20)] locally (see Appendix I for details)

$$\mathcal{B}^r_m(x,z) \sim -i2^{5/4}\left(\frac{k_0 L}{8\pi}\right)^{1/2} \frac{(\zeta_m - ib^r_m \cos\theta^i_m)}{(\tilde{R}^r_m)^{3/2}} \times \exp\left\{i\left[k\tilde{R}^r_m + x_m\left(\frac{\sin\theta^i_m}{\cos\alpha_m}\right) + ib^r_m + \frac{\pi}{4}\right]\right\} \tag{25}$$

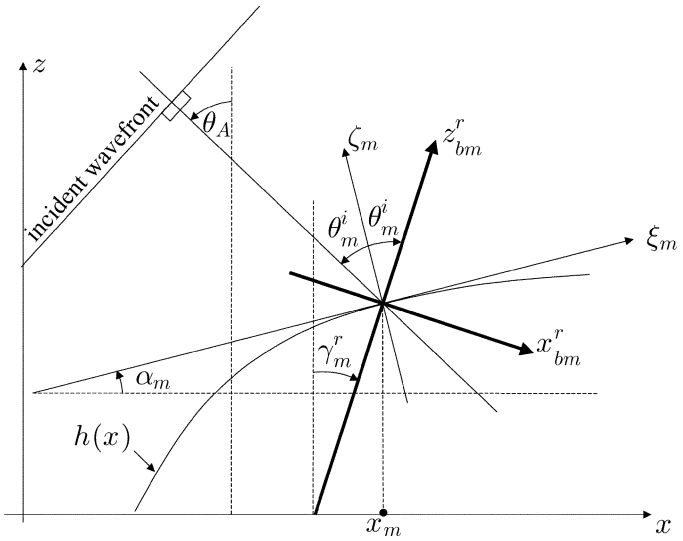

Fig. 3. Global and local coordinates for reflected beams. (x^r_{bm}, z^r_{bm}) is the mth reflected-beam coordinate system; (ξ_m, ζ_m) is the local tangent-normal coordinate system of Fig. 2, centered at lattice points $(x_m, h(x_m))$; $\alpha_m \equiv \alpha(x_m) = \tan^{-1}[dh(x_m)/dx]$ is the local slope; $\theta^i_m = \theta_A - \alpha(x_m)$ is the local incidence angle; $\gamma^r_m = \theta^i_m - \alpha_m$ is the local reflection angle measured from the z axis.

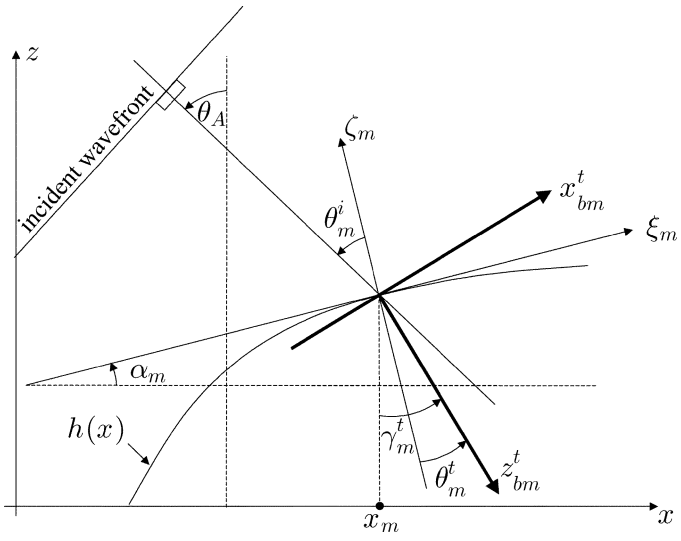

Fig. 4. As in Fig. 3, but for transmitted beams. (x^t_{bm}, z^t_{bm}) is the mth transmitted-beam coordinate system; θ^t_m is the local refraction angle measured from the surface normal; $\gamma^t_m = \theta^t_m + \alpha_m$ is the local refraction angle measured from the z axis. Note that for lossy materials, θ^t_m and γ^t_m are complex; for slight losses, the real (lossless) refraction angles in the figure are good approximations.

where (see Fig. 3) $\theta^i_m \equiv \theta^i(x_m)$, $\alpha_m \equiv \alpha(x_m)$

$$\zeta_m = -(x - x_m)\sin\alpha_m + [z - h(x_m)]\cos\alpha_m. \tag{26}$$

Furthermore

$$\tilde{R}^r_m = \sqrt{(x^r_{bm})^2 + (z^r_{bm} - ib^r_m)^2}, \qquad \mathrm{Re}\left(\tilde{R}^r_m\right) \geq 0 \tag{27}$$

is the complex distance, in the beam coordinates of Fig. 3, between the observation point

$$\begin{bmatrix} x^r_{bm} \\ z^r_{bm} \end{bmatrix} = \begin{bmatrix} \cos\gamma^r_m & -\sin\gamma^r_m \\ \sin\gamma^r_m & \cos\gamma^r_m \end{bmatrix} \begin{bmatrix} x - x_m \\ z - h(x_m) \end{bmatrix}, \qquad \gamma^r_m = \theta^i_m - \alpha_m = \theta_A - 2\alpha_m \tag{28}$$

and the CSP $(0, ib^r_m)$, with the complex displacement parameter b^r_m given by (generalizing [2, eq. (22)])

$$b^r_m = \frac{\left(L\cos\alpha_m\cos\theta^i_m\right)^2}{\lambda_0}. \tag{29}$$

In (25), and henceforth, the tilde ~ identifies dependence on analytically continued spatial source coordinates. The beam discretization in (22) with the CSP GB propagator in (25) is physically appealing because it represents a superposition of GBs launched from points $(x_m, h(x_m))$ on the illuminated portion of the interface along the reflection directions γ^r_m (see Fig. 3), which are *locally matched* to the surface EMSC. Similarly, for the transmitted GB propagator one obtains

$$\mathcal{B}^t_m(x,z) \sim i2^{5/4}\left(\frac{kL}{8\pi}\right)^{1/2} \frac{(\zeta_m - ib^t_m\cos\theta^t_m)}{(\tilde{R}^t_m)^{3/2}} \times \exp\left\{i\left[k\left(\tilde{R}^t_m + x_m\frac{\sin\theta^t_m}{\cos\alpha_m} + ib^t_m\right) + \frac{\pi}{4}\right]\right\} \tag{30}$$

where θ^t_m is the local refraction angle (see Fig. 4), related to θ^i_m and ϵ^e_r via Snell's law

$$\sin\theta^i_m = \sqrt{\epsilon^e_r}\sin\theta^t_m. \tag{31}$$

Moreover, in the beam coordinates of Fig. 4, $\tilde{R}^t_m$ is the complex distance

$$\tilde{R}^t_m = \sqrt{(x^t_{bm})^2 + (z^t_{bm} - ib^t_m)^2}, \qquad \mathrm{Re}\left(\tilde{R}^t_m\right) \geq 0 \tag{32}$$

with

$$\begin{bmatrix} x^t_{bm} \\ z^t_{bm} \end{bmatrix} = \begin{bmatrix} \cos\gamma^t_m & \sin\gamma^t_m \\ \sin\gamma^t_m & -\cos\gamma^t_m \end{bmatrix} \begin{bmatrix} x - x_m \\ z - h(x_m) \end{bmatrix} \qquad \gamma^t_m = \theta^t_m + \alpha_m \tag{33}$$

and the complex displacement parameter given by

$$b^t_m = \sqrt{\epsilon^e_r}\frac{(L\cos\alpha_m\cos\theta^t_m)^2}{\lambda_0}. \tag{34}$$

Like the reflected field, the transmitted field is synthesized via (22) and (30) with EMSC-*matched* CSP GBs propagating along the *local refraction direction* γ^t_m (see Fig. 4). Since the dielectric half-space is assumed to be lossy, θ^t_m, γ^t_m, and b^t_m are complex.

IV. TD Formulation

A. Preliminary Considerations

The FD beam propagators in (25) and (30) are nearly identical with that in [22, eq. (20)]. Therefore, extension to the TD for pulsed excitation can be pursued by following the procedure in [2, Sec. III-A]. However, the TD inversion is now complicated by the dispersive (ohmic) properties of the dielectric half-space [cf. (13)]. Although, analytic approaches to PB propagation in

ohmic-dispersive media are available [14], here we use a simpler approach, restricted to slightly lossy materials, i.e.,

$$\frac{\sigma}{\omega\epsilon_0\epsilon_r} \ll 1, \quad \omega < \Omega \tag{35}$$

with Ω denoting the effective bandwidth of the pulse $p(t)$. This condition is fulfilled for a class of actual ground penetrating radar (GPR) applications which is a topic of interest to us (see, e.g., the discussion in [15]), and which allows the complex wavenumber to be written as [15]

$$k = \frac{\omega}{c}\sqrt{\epsilon_r^e} \approx \sqrt{\epsilon_r}\frac{\omega}{c}\left(1 + i\frac{\sigma}{2\omega\epsilon_0\epsilon_r}\right) = \sqrt{\epsilon_r}\frac{\omega}{c} + i\frac{\sigma}{2c\epsilon_0\sqrt{\epsilon_r}} \tag{36}$$

i.e., with a *frequency-independent* (nondispersive) imaginary part. For example, a GPR system with 2 GHz center frequency and 1-GHz bandwidth, for a typical class of clay-loam soils ($\epsilon_r = 4.5$, $\sigma = 0.012$ S/m) [16], would have $\sigma/(\omega\epsilon_0\epsilon_r) \approx 0.05$ in (35) in the worst-case scenario. The nondispersive approximation considerably simplifies the TD inversion. In what follows, we shall be using (36) for calculating the transmitted field. Moreover, we approximate the frequency-dependent reflection coefficient in (12) by its (real, frequency independent) value at $\sigma = 0$

$$\mathcal{R}(x,\omega) \approx \mathcal{R}_0(x) \equiv \mathcal{R}(x,\omega)|_{\sigma=0}. \tag{37}$$

As in [2], we assume a frequency-independent Gabor lattice parameter L in order to conveniently estimate the TD Gabor coefficients by aperture sampling (see the discussion in [2, Sec. III-A]). Anticipating Fourier inversion, recalling (5), (11), (16), (18), and (37), the FD Gabor coefficients in (21) can be written as

$$C_m^\nu \approx 2c_m^\nu P(\omega)\exp(i\omega t_m) \qquad \nu = r \text{ or } t \tag{38}$$

where

$$\begin{aligned} c_m^r &= \left(\frac{L}{\sqrt{2}}\right)^{1/2} g(x_{Bm})\mathcal{R}_0(x_m) \\ c_m^t &= \left(\frac{L}{\sqrt{2}}\right)^{1/2} g(x_{Bm})\left[1 + \mathcal{R}_0(x_m)\right] \end{aligned} \tag{39}$$

are real and frequency independent, and

$$t_m = c^{-1}\left(\frac{z_{Bm} - x_m\sin\theta_m^i}{\cos\alpha_m}\right) \tag{40}$$

with (x_{Bm}, z_{Bm}) denoting the lattice points $(x_m, h(x_m))$ in the incident-beam coordinates (4)

$$\begin{bmatrix} x_{Bm} \\ z_{Bm} \end{bmatrix} = \begin{bmatrix} \cos\theta_A & \sin\theta_A \\ \sin\theta_A & -\cos\theta_A \end{bmatrix}\begin{bmatrix} x_m - x_A \\ h(x_m) - z_A \end{bmatrix}. \tag{41}$$

The FD Gabor expansions in (22) can thus be rewritten as

$$E^\nu(x,z,\omega) \sim \sum_{|m|\le(d/2L)} c_m^\nu P(\omega)\mathcal{B}_m^\nu(x,z,\omega)\exp(i\omega t_m), \quad \nu = r \text{ or } t. \tag{42}$$

As in [2], in order to deal with the evanescent spectra in the beam propagators $\mathcal{B}_m^r$ and $\mathcal{B}_m^t$, the TD is accessed by Fourier inversion of (42) via the analytic signal formulation [2, eqs. (31) and (32)], [17]

$$\overset{+}{f}(t) = \frac{1}{\pi}\int_0^\infty F(\omega)\exp(-i\omega t)d\omega, \quad \mathrm{Im}(t) \le 0 \tag{43}$$

where $F(\omega)$ is the conventional Fourier spectrum of the real signal $f(t)$, and the real signal for real t is recovered via

$$f(t) = \mathrm{Re}\left[\overset{+}{f}(t)\right]. \tag{44}$$

Accordingly [2, eq. (33)]

$$\overset{+}{e}{}^\nu(x,z,t) \sim \sum_{|m|\le(d/2L)} c_m^\nu \overset{+}{\mathrm{b}}{}_m^\nu(x,z,t-t_m) \ \nu = r \text{ or } t \tag{45}$$

with the analytic PB propagators $\overset{+}{\mathrm{b}}{}^\nu{}_m$ given by [2, eq. (34)]

$$\overset{+}{\mathrm{b}}{}^\nu{}_m(x,z,t) = \frac{1}{\pi}\int_0^\infty \mathcal{B}_m^\nu(x,z,\omega)P(\omega)\exp(-i\omega t)d\omega, \quad \mathrm{Im}(t) \le 0; \quad \nu = r \text{ or } t \tag{46}$$

and the real TD fields obtained from

$$e^\nu(x,z,t) = \mathrm{Re}\left[e^{\nu^+}(x,z,t)\right], \quad \nu = r \text{ or } t. \tag{47}$$

The analytic PB propagators $\overset{+}{\mathrm{b}}{}^r{}_m$ and $\overset{+}{\mathrm{b}}{}^t{}_m$ in (46) should not be confused with the complex displacement parameters b_m^r and b_m^t in (29) and (34), respectively.

As in [2], we consider a class of Rayleigh (differentiated Gaussian) pulses [2, eq. (37) and (38)]

$$p(t) = P_0\frac{d^j}{dt^j}\exp\left[-\left(\frac{t - \left(\frac{T}{2}\right)}{\varsigma T}\right)^2\right] \tag{48}$$

$$P(\omega) = \sqrt{\pi}P_0\varsigma T(-i\omega)^j\exp\left(-\frac{\varsigma^2\omega^2T^2}{4} + i\frac{\omega T}{2}\right) \tag{49}$$

where P_0 is a normalization constant, and the variance ς is chosen so that the pulse width of $p(t)$ is $\sim T$. We now generalize the TD results in [2, Sec. III-A], starting with the reflected field.

B. Reflected Field

As in [2], in order to evaluate the integral in (46) with (25) and (49), we first approximate the complex distance $\tilde{R}_m^r$ in (27), which is frequency dependent via (29). Assuming L/λ_0 (and therefore b_m^r) sufficiently small in the amplitude factor of (25) we let [2, eq. (39)]

$$\begin{aligned} \frac{(\zeta_m - ib_m^r\cos\theta_m^i)}{(\tilde{R}_m^r)^{3/2}} &\approx \frac{\zeta_m}{(R_m^r)^{3/2}} \\ R_m^r &= \sqrt{(x_{bm}^r)^2 + (z_{bm}^r)^2}, \\ b_m^r &\ll \zeta_m z_{bm}^r \end{aligned} \tag{50}$$

where R_m^r is real and frequency-independent, with ζ_m and (x_{bm}^r, z_{bm}^r) defined in (26) and (28), respectively. In the phase factor, instead of the paraxial approximation in [2, eq. (40)],

we use a perturbation (first-order McLaurin) approximation in terms of b_m^r [see (27) and (29)]

$$\begin{aligned}\tilde{R}_m^r(\omega) \approx & R_m^r - ib_m^r \frac{z_{bm}^r}{R_m^r} \\ = & R_m^r - i\omega \frac{z_{bm}^r (L\cos\alpha_m \cos\theta_m^i)^2}{2\pi c R_m^r}, \\ & b_m^r \ll z_{bm}^r \end{aligned} \tag{51}$$

which was found to give better results. Using (50) and (51), the beam propagator in (25) can be rewritten as

$$\mathcal{B}_m^r(x,z,\omega) \sim \Lambda_m^r \omega^{1/2} \exp\left[-\frac{(\omega T_m^r)^2}{4} + i\omega\tau_m^r\right] \tag{52}$$

where

$$\Lambda_m^r = -i2^{5/4} \exp\left(\frac{i\pi}{4}\right) \sqrt{\frac{L}{8\pi c}} \frac{\zeta_m}{(R_m^r)^{3/2}} \tag{53}$$

$$\begin{aligned}\tau_m^r = & c^{-1}\left(R_m^r + \frac{x_m \sin\theta_m^i}{\cos\alpha_m}\right) \\ T_m^r = & c^{-1}\left(L\cos\alpha_m\cos\theta_m^i\right)\sqrt{\frac{2}{\pi}\left(1-\frac{z_{bm}^r}{R_m^r}\right)}. \end{aligned} \tag{54}$$

Substituting (49) and (52) into (46), one obtains a canonical integral [18]

$$\begin{aligned} I(p,q,j) = & \int_0^\infty \omega^{j+1/2} \exp\left(ip\omega - \frac{q^2\omega^2}{4}\right) d\omega \\ = & 2^{j+1/2} q^{-j-5/2} \\ & \times \left[q\Gamma\left(\frac{3+2j}{4}\right) M_1^{(j)}\left(\frac{p}{q}\right) \right. \\ & \left. + 2ip\Gamma\left(\frac{5+2j}{4}\right) M_2^{(j)}\left(\frac{p}{q}\right)\right], \\ & q \in R^+ \end{aligned} \tag{55}$$

where $\Gamma(\cdot)$ is the gamma function [19], and

$$\begin{aligned} M_1^{(j)}(t) = & {}_1F_1\left(\frac{3+2j}{4}, \frac{1}{2}, -t^2\right) \\ M_2^{(j)}(t) = & {}_1F_1\left(\frac{5+2j}{4}, \frac{3}{2}, -t^2\right) \end{aligned} \tag{56}$$

with ${}_1F_1(u,v,t)$ denoting the Kummer confluent hypergeometric function [19]. The reflected analytic PB propagator can be thus written as

$$\begin{aligned} \overset{+}{b}{}^r{}_m(x,z,t) = & (-i)^j \beta_m^r \\ & \times \left[\mathcal{T}_m^r \Gamma\left(\frac{3+2j}{4}\right) \right. \\ & \times M_1^{(j)}\left(\frac{t-\tau_m^r-\left(\frac{T}{2}\right)}{\mathcal{T}_m^r}\right) \\ & -2i\left(t-\tau_m^r-\left(\frac{T}{2}\right)\right)\Gamma\left(\frac{5+2j}{4}\right) \\ & \left. \times M_2^{(j)}\left(\frac{t-\tau_m^r-\left(\frac{T}{2}\right)}{\mathcal{T}_m^r}\right)\right] \end{aligned} \tag{57}$$

where

$$\begin{aligned} \beta_m^r = & 2^{j+1/2}\pi^{-1/2}(\mathcal{T}_m^r)^{-j-5/2}\Lambda_m^r P_0 \varsigma T \\ \mathcal{T}_m^r = & \sqrt{(T_m^r)^2 + \varsigma^2 T^2}. \end{aligned} \tag{58}$$

Equation (57) generalizes [2, eq. (44)] to arbitrary order j of the derivative in (48). The functions $M_{1,2}^{(j)}$ can be efficiently computed using the rapidly converging expansions in Appendix II.

C. Transmitted Field

The transmitted PB propagator can be obtained similarly. The only slight difference is due to the complex wavenumber k and the complex parameters θ_m^t and b_m^t in (30) [see (31) and (34)]. For slightly lossy materials as in (35), the complex wavenumber is approximated via (36), whereas θ_m^t and b_m^t are approximated by the real values

$$\begin{aligned} \theta_m^t \approx & \theta_{m0}^t \equiv \sin^{-1}\left(\frac{\sin\theta_m^i}{\sqrt{\epsilon_r}}\right) \\ b_m^t \approx & b_{m0}^t \equiv \sqrt{\epsilon_r}\frac{(L\cos\alpha_m\cos\theta_{m0}^t)^2}{\lambda_0}. \end{aligned} \tag{59}$$

Accordingly

$$\begin{aligned} \overset{+}{\mathrm{b}}{}^t{}_m(x,z,t) = & (-i)^j \beta_m^t \\ & \times \left[\mathcal{T}_m^t \Gamma\left(\frac{3+2j}{4}\right) M_1^{(j)}\left(\frac{t-\tau_m^t-\left(\frac{T}{2}\right)}{\mathcal{T}_m^t}\right) \right. \\ & -2i\left(t-\tau_m^t-\left(\frac{T}{2}\right)\right)\Gamma\left(\frac{5+2j}{4}\right) \\ & \left. \times M_2^{(j)}\left(\frac{t-\tau_m^t-\left(\frac{T}{2}\right)}{\mathcal{T}_m^t}\right)\right] \end{aligned} \tag{60}$$

where

$$\begin{aligned} \beta_m^t = & 2^{j+1/2}\pi^{-1/2}\left(\mathcal{T}_m^t\right)^{-j-5/2}\Lambda_m^t P_0 \varsigma T \\ \mathcal{T}_m^t = & \sqrt{\left(T_m^t\right)^2 + \varsigma^2 T^2} \end{aligned} \tag{61}$$

$$\begin{aligned} \Lambda_m^t = & i(\epsilon_r)^{1/4} 2^{5/4} \\ & \times \exp\left(-\kappa R_{m0}^t + \frac{i\pi}{4}\right)\sqrt{\frac{L}{8\pi c}}\frac{\zeta_m}{\left(R_{m0}^t\right)^{3/2}} \\ \kappa = & \frac{\sigma}{2c\epsilon_0\sqrt{\epsilon_r}} \end{aligned} \tag{62}$$

$$\begin{aligned} \tau_m^t = & c^{-1}\left[\sqrt{\epsilon_r}\left(\frac{R_{m0}^t + x_m\sin\theta_{m0}^t}{\cos\alpha_m}\right)\right] \\ T_m^t = & c^{-1}\left(L\cos\alpha_m\cos\theta_{m0}^t\right) \\ & \times \sqrt{\frac{2\epsilon_r}{\pi}\left(1-\frac{z_{bm0}^t}{R_{m0}^t}\right)} \end{aligned} \tag{63}$$

$$\begin{aligned} R_{m0}^t = & \sqrt{\left(x_{m0}^t\right)^2 + \left(z_{m0}^t\right)^2} \\ \begin{bmatrix} x_{bm0}^t \\ z_{bm0}^t \end{bmatrix} = & \begin{bmatrix} \cos\gamma_{m0}^t & \sin\gamma_{m0}^t \\ \sin\gamma_{m0}^t & -\cos\gamma_{m0}^t \end{bmatrix} \begin{bmatrix} x - x_m \\ z - h(x_m) \end{bmatrix} \\ \gamma_{m0}^t = & \theta_{m0}^t + \alpha_m. \end{aligned} \tag{64}$$

D. Limitations

The limitations of the proposed approach can be divided into two categories. The first category includes the *model constraints*, i.e., the underlying PO approximation and all other simplifying assumptions. These constraints are known *a priori*, and can be summarized as follows:

1) moderately rough interfaces (both in height and slope) with local curvature radii large compared to the pulse length cT;
2) plane-wave excitation [cf. (3)] with incidence direction far from grazing;
3) slightly lossy dielectrics [cf. (35)].

Strong roughness and/or near-grazing incidence would require more sophisticated models than the simple PO approximation in Section III-A. More general (e.g., focused) excitations would require a two-step procedure: first discretizing the aperture field distribution in terms of narrow-waisted GBs as in [2] and subsequently applying the PO algorithm to each incident beam. Concerning more sophisticated loss/dispersion models in the TD, one possibility is the inclusion of ohmic dispersion, which can be accommodated within the analytic framework of Gaussian PBs [14].

The second type of constraint is related to the adequacy of the narrow-waisted PB discretization in Section IV-B and C, in terms of the number of beams required to guarantee stability of the outcome. We have referred to this as the *scrambling* criterion, i.e., the insensitivity of the result with respect to different combinations of the beam/lattice configuration. Overall reliability requires that both the model constraints and the scrambling criterion are satisfied.

V. Numerical Results

A. Reference Solution

The PB syntheses presented in Section IV have been validated and calibrated against an independent reference solution based on the time-harmonic multifilament current method in [20], and adapted to moderately rough interfaces (cf. [1, App. B]). The frequency spectra of the reflected and transmitted fields were obtained by solving the FD problem at 100 different frequencies within the pulse bandwidth. The incident FD field was computed via numerical integration of the rigorous Kirchhoff aperture distribution [the spectrum of (2)], without resorting to the plane wave approximation, and with use of the full dispersive permittivity model in (13) for the dielectric half-space. The resulting frequency samples were smoothed through local Padé approximation [21] and filtered by the pulse spectrum $P(\omega)$ in (49). The TD solution was then obtained via standard inverse FFT routines [21].

B. Simulation Parameters

The numerical simulations that follow are based on the pulsed aperture field distribution in (2) with the Gaussian taper

$$g(x) = \exp\left[\frac{-18x^2}{(d\cos\theta_A)^2}\right] \tag{65}$$

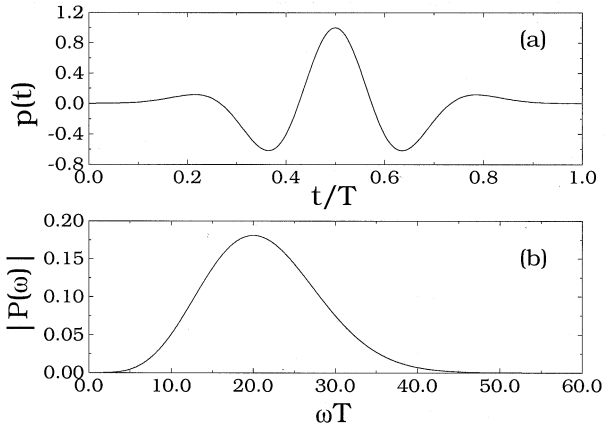

Fig. 5. Fourth-order Rayleigh pulse. (a) Temporal profile in (48). (b) Spectrum (magnitude) in (49) ($j = 4$, $P_0 = T^4/30\,000$, $\varsigma = 1/\sqrt{50}$).

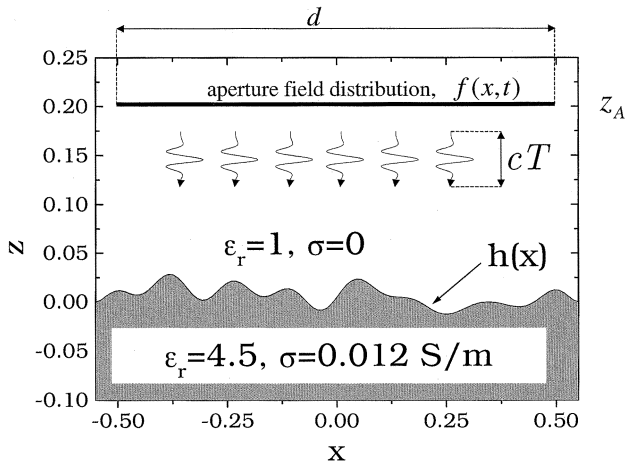

Fig. 6. Simulation geometry (cf. Fig. 1) and parameters (arbitrary units). Aperture field distribution in (2), with (65): $d = 1$, $\theta_A = 0$, $x_A = 0$, $z_A = 0.2$, and $p(t)$ as in Fig. 5 with $cT = 0.08$. Rough surface profile: maximum height $h_{\max} = 0.36cT$; maximum slope $\alpha_{\max} = 31°$; average curvature radius $\bar{r}_c = 5.9cT$. Dielectric parameters: $\epsilon_r = 4.5$, $\sigma = 0.012$ S/m.

and the wide-band fourth-order Rayleigh pulse $p(t)$, obtained from (48) with $j = 4$, $P_0 = T^4/30\,000$, $\varsigma = 1/\sqrt{50}$, and length $cT = 0.08d$ [see Fig. 5(a)], which has a center angular frequency $\Omega_0 = 20/T$ [Fig. 5(b)]. For the reflected/transmitted fields, the special functions $M_{1,2}^{(4)}$ in (57) and (60) were computed via the rapidly converging expansions in Appendix B with $N = 5$ (cf. [2, eq. (50–51)]). The aperture height z_A was chosen so as to place the rough dielectric interface within the collimation zone of the aperture, thereby justifying the plane-wave incidence approximation in (3); depending on the tilt angle θ_A, the spatial shift x_A was adjusted so that the illuminated region was confined in the interval $[-d/2, d/2]$ [see Fig. 1(b)]. In each of the examples below, it was verified that the illumination at the edges $x = \pm d/2$ was at least 30 dB below the maximum strength so that numerical artifacts due to edge effects were negligible. The rough surface profile was generated via the quartic spline model in [1]. For the GPR applications of interest in our studies, the dielectric half-space parameters were chosen so as to simulate a class of realistic soils (Puerto Rican clay loam [16]), with the frequency range chosen to satisfy (35).

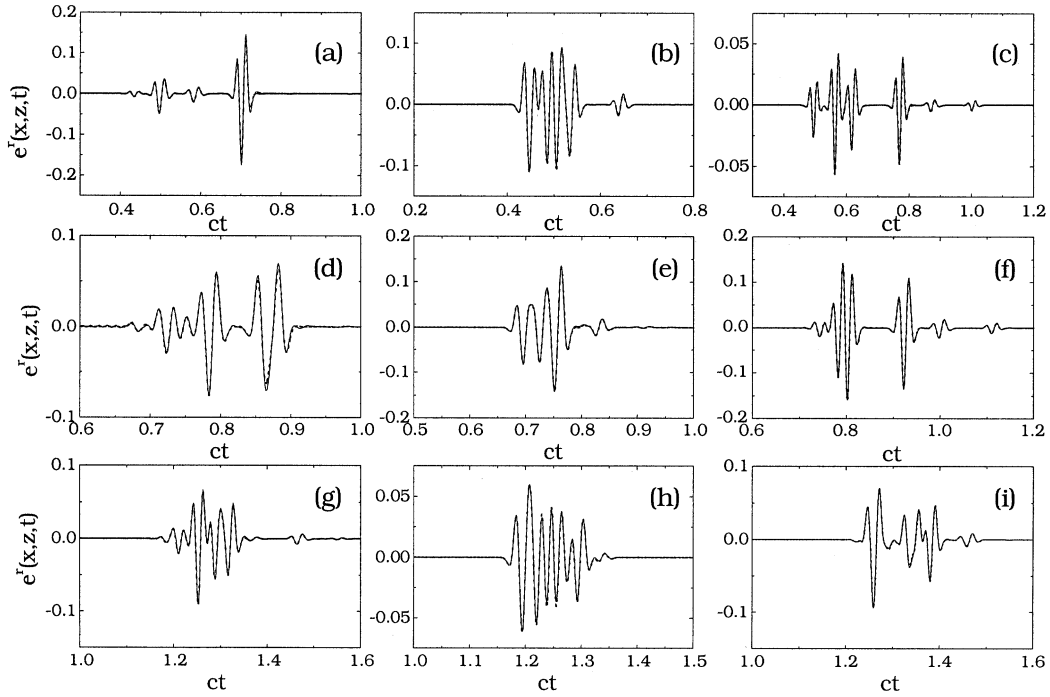

Fig. 7. Reflected field at various observation points. Parameters as in Fig. 6. (a)–(c) $z = 0.25, x = -0.4, 0, 0.4$, respectively. (d)–(f): $z = 0.5, x = -0.4, 0, 0.4$, respectively. (g)–(i): $z = 1$, $x = -0.4, 0, 0.4$, respectively. — Reference solution; - - - Beam synthesis ($d/L = 150$, i.e., 150 beams).

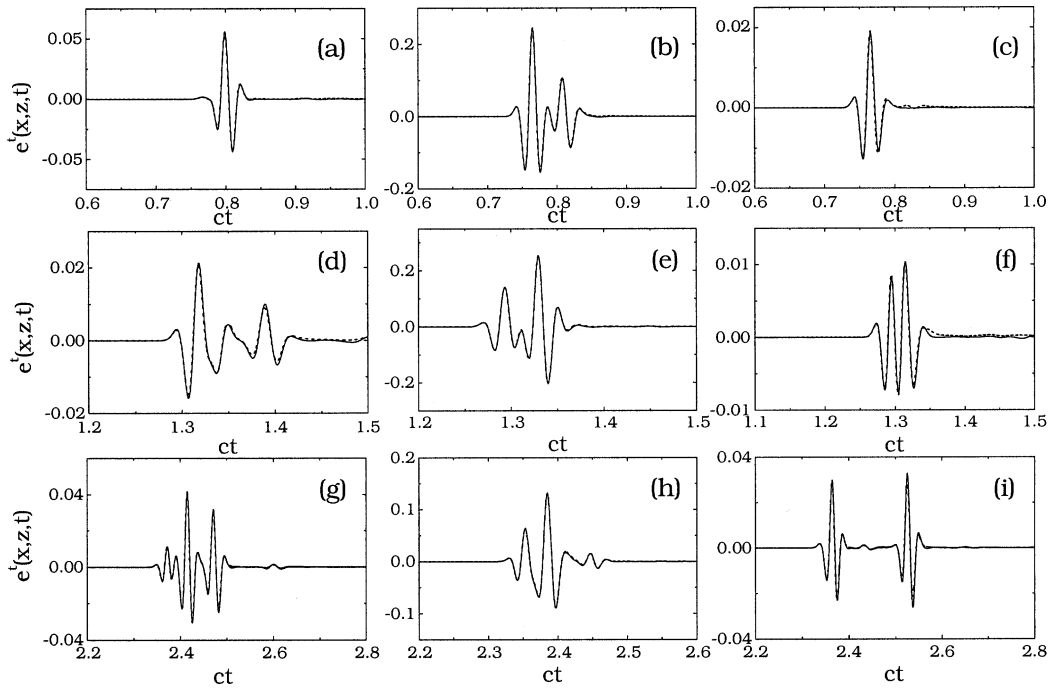

Fig. 8. Transmitted field at various observation points. Parameters as in Fig. 6. (a)–(c) $z = -0.25, x = -0.4, 0, 0.4$, respectively; (d)–(f) $z = -0.5, x = -0.4$, 0, 0.4, respectively; (g)–(i): $z = -1, x = -0.4, 0, 0.4$, respectively. — Reference solution; - - - Beam synthesis ($d/L = 150$, i.e., 150 beams).

C. Results

We begin with the problem geometry in Fig. 6, with the relevant parameters specified in the figure caption. For this configuration, the roughness is moderate both in height ($h_{\max} = 0.36cT$) and slope ($\alpha_{\max} = 31°$), and the average radius of curvature $\bar{r}_c$ is large with respect to the pulse length ($\bar{r}_c = 5.9cT$). The incident field direction is vertical ($\theta_A = 0$), and the constitutive parameters ϵ_r, σ satisfy (35). The previously stated conditions for validity of the proposed PB synthesis in (47) should be thus satisfied, and good accuracy should be expected with an "adequate" number of beams. The reflected and transmitted fields have been computed via (47) with (57) and (60), respectively, at nine observation points (three different horizontal positions, spanning the illuminated region, on three observation planes). The reflected/transmitted temporal waveforms obtained

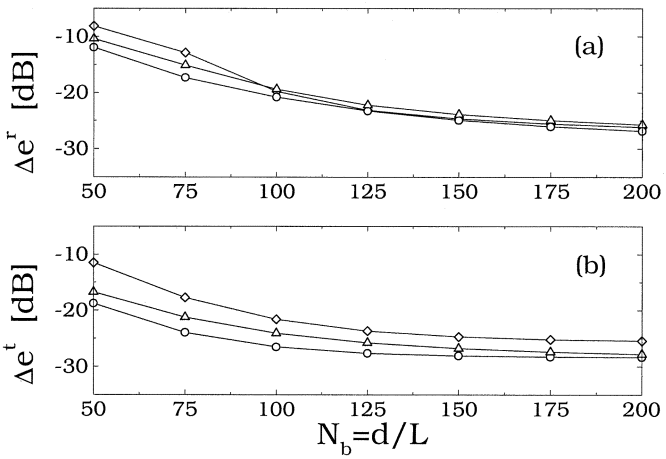

Fig. 9. rms errors $\Delta e^{r,t}$ in (66) versus number of beams $N_b = d/L$ at various observation points. Parameters as in Fig. 6. (a) Reflected field. (b) Transmitted field. —◇—: $x = 0$, $z = \pm 0.25$; —○—: $x = 0$, $z = \pm 0.5$; —△—: $x = 0$, $z = \pm 1$.

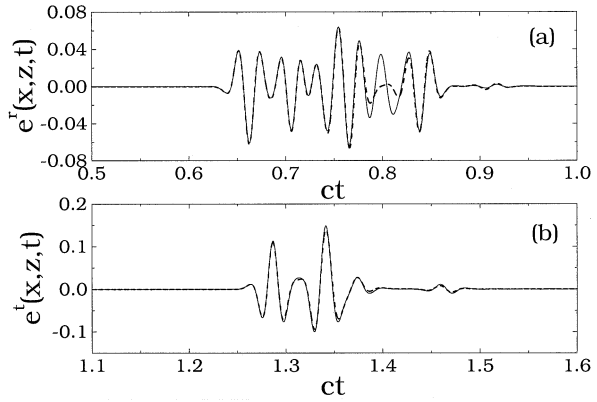

Fig. 10. Parameters as in Fig. 6, but with roughness profile scaled so that $h_{\max} = 0.6cT$, $\alpha_{\max} = 46°$, $\bar{r}_c = 4.4cT$. (a) Reflected field at $x = 0$, $z = 0.5$: (b) Transmitted field at $x = 0$, $z = -0.5$. — Reference solution; - - - Beam synthesis ($d/L = 200$, i.e., 200 beams). rms errors: $\Delta e^r = -10$ dB, $\Delta e^t = -20$ dB.

via the PB synthesis with 150 beams are shown in Figs. 7 and 8, respectively, and are compared with the reference solution. Very good agreement is observed. At certain observation points, especially at smaller observation distance [cf. Fig. 7(a), (c), and (f)], the dominant contributions turn out to be well separated and replicate the incident waveform (inverted due to reflection). This is not the case in the central region ($x = 0$), where the almost simultaneous arrivals from the surface do not allow their separate resolution for the specified input pulse width, thereby resulting in the chirped oscillations in Fig. 7(b), (e), and (h). Separate (noninverted) arrivals are also visible in the transmitted field [cf. Fig. 8(i)]; at smaller observation distance [e.g., Fig. 8(a) and (c)], however, the transmitted field waveforms coalesce into a close replication of the incident pulse. In all examples, the PB syntheses and the numerical reference solutions are in close agreement, thereby, demonstrating the high-resolution capabilities of the PB algorithm under controlled conditions.

The number of beams in these examples were arrived at using the pragmatic stability criterion discussed in Section IV-D. In order to better quantify the accuracy, and address convergence issues, we have computed the rms (energy) errors in (66), shown at the bottom of the page, where the subscript $_r$ denotes the reference solution and $_b$ denotes the PB synthesis. The rms errors for Figs. 7 and 8 are < -25 dB. The convergence of the algorithm in Figs. 7 and 8 is illustrated in Fig. 9, where the rms errors for both reflected and transmitted fields are plotted versus the number of beams $N_b = d/L$. The various curves pertain to different observation points. It is noted that beyond a critical threshold, the error becomes *practically insensitive* to a further increase in the number of beams, indicating that convergence has been achieved. "Convergence" here implies that the *PO integral* is adequately beam-discretized but, as noted in Section IV-D, this *does not* necessarily imply that the *overall* solution is accurate; good *overall* accuracy requires that the model constraints are likewise satisfied. The test configuration was chosen deliberately so that this is the case. In this example, the convergence turns out to be weakly dependent on the observation point, and a robust threshold for *uniformly* good accuracy ($\Delta e^{r,t} \lesssim -25$ dB) can be set around $N_b = 150$. If the *model constraints* in Section IV-D were violated, the PB synthesis, although stabilized, could be *inaccurate*. For illustration, we strained the algorithm by selecting simulation parameters near the limit of their range of validity. The results in Fig. 10 pertain to the profile in Fig. 6, conformally scaled so as to increase the roughness up to a maximum height $h_{\max} = 0.6cT$ and a maximum slope $\alpha_{\max} = 46°$, with an average curvature radius $\bar{r}_c = 4.4cT$. The number of beams was chosen to satisfy the stability criterion. Remarkably, the PB synthesis still performs well, but now one observes discrepancies with respect to the reference solution [particularly in one late-time peak in Fig. 10(a)] which *cannot* be repaired by increasing the number of beams. Note that the increased roughness admits multiple reflections which are accounted for in the reference solution but ignored in the PO algorithm. This may contribute to the diminished accuracy, which now yields rms errors $\Delta e^r = -10$ dB, $\Delta e^t = -20$ dB. The deterioration is aggravated further for oblique incidence, where multiple interactions are more pronounced, as seen in Fig. 11, where the profile of Fig. 10 is illuminated by a tilted beam with $\theta_A = 40°$. For this example, $\Delta e^r = -8$ dB and $\Delta e^t = -9$ dB. We also investigated the accuracy degradation in the "low-frequency" (i.e., long pulse) limit. As an illustration, the reflected and transmitted waveforms at various observation points in Fig. 12 pertain to the geometry in Fig. 6, but using a ten-times longer excitation pulse ($cT = 0.8$). For this configuration, $cT = 0.8d$ and $\bar{r}_c = 0.59cT$; the

$$\Delta e^{\nu} = \frac{\int_{-\infty}^{\infty} |e_r^{\nu}(x,z,t) - e_b^{\nu}(x,z,t)|^2 \, dt}{\left[\int_{-\infty}^{\infty} |e_r^{\nu}(x,z,t)|^2 \, dt \int_{-\infty}^{\infty} |e_b^{\nu}(x,z,t)|^2 \, dt\right]^{1/2}}, \qquad \nu = r \text{or } t \tag{66}$$

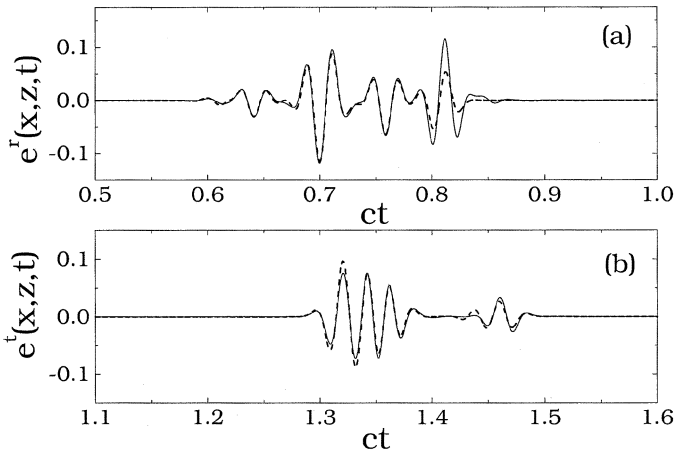

Fig. 11. As in Fig. 10, but oblique incidence with $\theta_A = 40^\circ$ and $x_A = -z_A \tan\theta_A$. — Reference solution; - - - Beam synthesis ($d/L = 200$, i.e., 200 beams). rms errors: $\Delta e^r = -8$ dB, $\Delta e^t = -9$ dB.

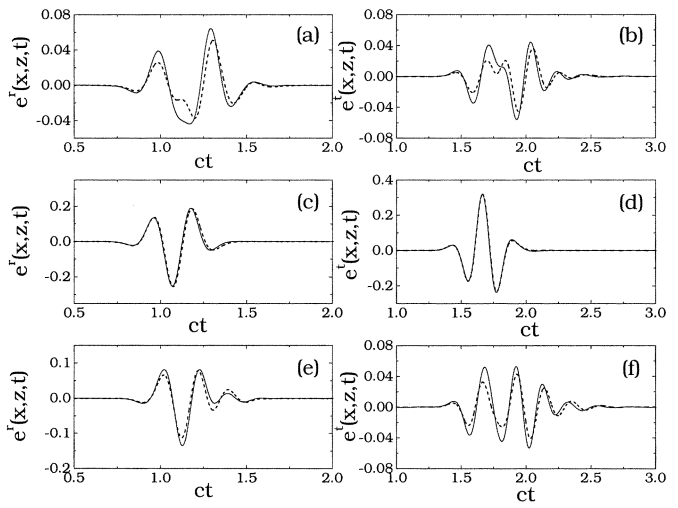

Fig. 12. Parameters as in Fig. 6, but with longer pulse, $cT = 0.8$ ($h_{\max} = 0.036cT$, $\bar{r}_c = 0.59cT$). (a), (c), and (e). Reflected field at $z = 0.5$ and $x = -0.4, 0., 0.4$, respectively (rms errors $\Delta e^r = -6, -16, -11$ dB, respectively). (b), (d), and (f): Transmitted field at $z = -0.5$ and $x = -0.4, 0, 0.4$, respectively (rms error $\Delta e^t = -5, -25, -7$ dB, respectively). — Reference solution; - - - beam synthesis ($d/L = 30$, i.e., 30 beams).

reduced radius of curvature stretches the validity of the asymptotics in the PO model and in the CSP approximations (25) and (30). First, one notes from Fig. 12 that the reflected/transmitted waveforms contain less structure than those in Figs. 7, 8,10, and 11, since the surface is now *flatter* on the pulse length scale ($h_{\max} = 0.036cT$). Second, due to the lower-frequency content of the pulse, recalling (29) and (51), a larger Gabor lattice period L (i.e., fewer beams) should be adequate to stabilize the beam synthesis. This was confirmed in numerical simulations, where the beam syntheses were found to stabilize around $N_b = 30$. As seen from Fig. 12, the beam syntheses, though reasonably good, are no longer *highly* accurate, but have rms errors ranging from -25 dB to -5 dB. As in Figs. 10 and 11, the accuracy *cannot* be improved by increasing the number of beams, indicating that the limit in range of validity of the PO/CSP asymptotics has been reached. The results above highlight the GPR tradeoff between resolution (achievable by shortening the pulse) and adequate soil penetration (achievable with lower-frequency excitation). Specific numerical values are application-dependent, and are discussed in [22] and [23] in connection with imaging of shallowly buried low-contrast plastic landmines. We found that for practical ultrawide-band applications, the nondispersive approximation in (35) and (36) works reasonably well. From a practical viewpoint, we have found fairly accurate predictions ($\Delta e^{r,t} \lesssim -20$ dB) for roughness with maximum height $h_{\max} \lesssim 0.5cT$, (average) curvature radii $\bar{r}_c \lesssim 2cT$, maximum slopes $\alpha_{\max} \lesssim 40^\circ$, for nearly-vertical incidence ($\theta_A \lesssim 30^\circ$), and for dielectrics with $\sigma/(\Omega_0\epsilon_0\epsilon_r) \lesssim 0.05$. For the examples in Figs. 7, 8, 10, and 11, 150–200 beams were usually found to be sufficient to reach convergence, resulting in negligible memory requirements and an average computing time of $T_c = 6$ ms per field time sample (at a fixed observation point) on a 700-MHz PC. Note that the computing time scales linearly with the number of beams; accordingly, for the examples in Fig. 12 (i.e., 30 beams) we found $T_c = 1$ ms. These computational features look quite attractive when compared with those of typical full-wave solvers. A rough estimate of the average computing time for our reference solution as described in Section V-A (which, however, was not fully optimized) is on the order of 2 s per space-time sample, with memory requirements on the order of 10 MB.

VI. Conclusion

A Gabor-based quasi-ray PB algorithm has been presented for a short-pulse 2-D reflection by, and transmission through, a 1-D moderately rough interface separating free space from a slightly-lossy dielectric half-space. The approach is based on the Kirchhoff PO approximation and the PB 1-D aperture field discretization in [2], and has been validated and calibrated against an independently generated reference solution. Numerical simulations show that the proposed algorithm yields robust and accurate predictions in a calibrated range of parameters, and is fairly attractive in terms of computational features when compared with full-wave rigorous solvers. Extensions to more general dispersion/loss models and to noncollimated aperture excitations remain to be investigated (for one possibility, see [14]). Extension to 2-D surfaces, and 3-D field scattering, based on 2-D aperture PB discretization [24], is currently under consideration. The algorithm has already been applied to inverse scattering scenarios involving moderately rough surface-profile estimation [22] for enhanced subsurface-target imaging. Preliminary results for imaging of shallowly buried low-contrast plastic targets look encouraging [23].

Appendix I
Details Pertaining to (25)

For narrow Gaussian windows, with $L \lesssim \lambda_0 \ll d$, the integrand in (23) is strongly localized around $x = x_m$. Thus, for moderate roughness, the integration path near x_m can be approximated by the local tangent plane, and the phase function can be assumed to be linear. Accordingly, in the (ξ_m, ζ_m) coor-

dinate system of Fig. 3

$$\begin{bmatrix}\xi_m\\ \zeta_m\end{bmatrix}=\begin{bmatrix}\cos\alpha_m & \sin\alpha_m\\ -\sin\alpha_m & \cos\alpha_m\end{bmatrix}\begin{bmatrix}x-x_m\\ z-h(x_m)\end{bmatrix},\qquad \alpha_m\equiv\alpha(x_m) \tag{67}$$

the reflected-beam integral in (23) can be approximated as

$$\mathcal{B}_m^r(x,z)\approx -2\int_{-\infty}^{\infty} w_{\alpha m}(\xi_m')\,\frac{\partial}{\partial\zeta_m}G_{2D}(\xi_m,\zeta_m;\xi_m',0;k_0)\times\exp[ik_0\left(\frac{\xi_m'+x_m}{\cos\alpha_m}\right)\sin\theta_m^i]d\xi_m' \tag{68}$$

where $w_{\alpha m}(\cdot)$ is the Gaussian window in (20) projected onto the local tangent plane (ξ_m axis in Fig. 3)

$$w_{\alpha m}(x)=w\left(\frac{x}{\cos\alpha_m}\right)=\left(\frac{\sqrt{2}}{L}\right)^{1/2}\times\exp\left[-\pi\left(\frac{x}{L\cos\alpha_m}\right)^2\right]. \tag{69}$$

The integral in (68) has the same form as [2, eq. (9)]. Therefore, straightforward application of the paraxial far zone approximation detailed in [7, Appendix] yields the result in (25). Similar considerations applied to the transmitted beams in (24) yield (30) (see Fig. 4).

Appendix II

Rapidly Converging Expansions for $M_{1,2}^{(j)}$

As in [2, Appendix C], using the Kummer transformation and the truncated Taylor series for the confluent hypergeometric function ${}_1F_1$, one obtains [19]

$$M_1^{(j)}(t)=\exp(-t^2)\,{}_1F_1\left(-\frac{1+2j}{4},\frac{1}{2},t^2\right)\approx\exp(-t^2)\sum_{n=0}^{N}\frac{\left(-\frac{1+2j}{4}\right)_n}{\left(\frac{1}{2}\right)_n n!}t^{2n} \tag{70}$$

$$M_2^{(j)}(t)=\exp(-t^2)\,{}_1F_1\left(\frac{1-2j}{4},\frac{3}{2},t^2\right)\approx\exp(-t^2)\sum_{n=0}^{N}\frac{\left(\frac{1-2j}{4}\right)_n}{\left(\frac{3}{2}\right)_n n!}t^{2n} \tag{71}$$

with $(u)_n$ denoting the Pochammer symbol [19]

$$(u)_n=u(u+1)(u+2)\ldots(u+n-1),\qquad (u)_0=1. \tag{72}$$

As shown in [2, Fig. 5], the expansions in (70) and (71) guarantee satisfactory accuracy with few terms ($N\approx 5$).

References

[1] V. Galdi, L. B. Felsen, and D. A. Castañon, "Quasiray Gaussian beam algorithm for time-harmonic two-dimensional scattering by moderately rough interfaces," *IEEE Trans. Antennas Propagat.*, vol. 49, pp. 1305–1314, Sept. 2001.

[2] ——, "Narrow-waisted Gaussian beam discretization for short-pulse radiation from one-dimensional large apertures," *IEEE Trans. Antennas Propagat.*, vol. 49, pp. 1322–1332, Sept. 2001.

[3] J. Baldauf, S. W. Lee, H. Ling, and R. Chou, "On physical optics for calculating scattering from coated bodies," *J. Electromagn. Waves Appl.*, vol. 3, no. 8, pp. 725–746, Aug. 1989.

[4] T. Dogaru and L. Carin, "Time-domain sensing of targets buried under a rough air-ground interface," *IEEE Trans. Antennas Propagat.*, vol. 46, pp. 360–372, Mar. 1998.

[5] G. A. Tsihrintzis, C. M. Rappaport, S. C. Winton, and P. M. Johansen, "Statistical modeling of rough surface scattering for ground-penetrating radar applications," *Detection Remediation Technology for Mines and Mine-Like Targets III, Proc. SPIE*, vol. 3392, pp. 735–744, 1998.

[6] T. Dogaru and L. Carin, "Multiresolution time domain analysis of scattering from a rough dielectric surface," *Radio Sci.*, vol. 35, no. 6, pp. 1279–1292, Nov.–Dec. 2000.

[7] J. J. Maciel and L. B. Felsen, "Gaussian beam analysis of propagation from an extended aperture distribution through dielectric layers, Part I—Plane layer," *IEEE Trans. Antennas Propagat.*, vol. 38, pp. 1607–1617, Oct. 1990.

[8] ——, "Gaussian beam analysis of propagation from an extended aperture distribution through dielectric layers, Part II—Circular cylindrical layer," *IEEE Trans. Antennas Propagat.*, vol. 38, pp. 1618–1624, Oct. 1990.

[9] R. F. Harrington, "On scattering by large conducting bodies," *IRE Trans. Antennas Propagat.*, pp. 150–153, Apr. 1959.

[10] E. I. Thorsos, "The validity of the Kirchhoff approximation for rough surface scattering using a Gaussian roughness spectrum," *J. Acoust. Soc. Amer.*, vol. 83, pp. 78–82, Aug. 1988.

[11] A. Collaro, G. Franceschetti, M. Migliaccio, and D. Riccio, "Gaussian rough surfaces and Kirchhoff approximation," *IEEE Trans. Antennas Propagat.*, vol. 47, pp. 392–398, Feb. 1999.

[12] G. Franceschetti, A. Iodice, M. Migliaccio, and D. Riccio, "Scattering from natural rough surfaces modeled by fractional Brownian motion two-dimensional processes," *IEEE Trans. Antennas Propagat.*, vol. 47, pp. 1405–1415, Sept. 1999.

[13] J. A. DeSanto and G. S. Brown, "Analytical techniques for multiple scattering from rough surfaces," in *Progress in Optics XXIII*, E. Wolf, Ed. Amsterdam: North-Holland, 1986.

[14] E. Heyman, A. G. Tijhuis, and J. Boersma, "Spherical and collimated pulsed fields in conducting media," in *Proc. URSI Trianum Int. Symp. Electromagnetic Theory*, St. Petersburg, Russia, 1995, pp. 643–645.

[15] T. B. Hansen and P. M. Johansen, "Inversion scheme for ground penetrating radar that takes into account the planar air-soil interface," *IEEE Trans. Geosci. Remote Sensing*, vol. 38, pp. 496–506, Jan. 2000.

[16] J. E. Hipp, "Soil electromagnetic parameters as functions of frequency, soil density, and soil moisture," *Proc. IEEE*, vol. 62, pp. 98–103, Jan. 1974.

[17] T. B. Hansen and A. D. Yaghjian, *Plane-Wave Theory of Time-Domain Fields: Near-Field Scanning Applications*. Piscataway, NJ: IEEE Press, 1999.

[18] S. Wolfram, *The Mathematica Book*, 3rd ed. New York: Wolfram Media/Cambridge Univ. Press, 1996.

[19] M. Abramowitz and I. A. Stegun, *Handbook of Mathematical Functions*. New York: Dover, 1964.

[20] Y. Leviatan and A. Boag, "Analysis of electromagnetic scattering from dielectric cylinders using a multifilament current model," *IEEE Trans. Antennas Propagat.*, vol. 35, pp. 1119–1127, Oct. 1987.

[21] W. H. Press, S. A. Teukolsky, W. T. Vetterling, and B. P. Flannery, *Numerical Recipes in C: The Art of Scientific Computing*, 2nd ed. Cambridge, UK: Cambridge Univ. Press, 1992.

[22] V. Galdi, J. Pavlovich, W. C. Karl, D. A. Castañon, and L. B. Felsen, "Moderately rough dielectric interface reconstruction via short-pulse quasiray Gaussian beams," *IEEE Trans. Antennas Propagat.*, Mar. 2003, to be published.

[23] V. Galdi, H. Feng, D. A. Castañon, W. C. Karl, and L. B. Felsen, "Moderately rough surface underground imaging via short-pulse quasiray gaussian beams," *IEEE Trans. Antennas Propagat.*, Sept. 2003, to be published.

[24] V. Galdi, L. B. Felsen, and D. A. Castañon, "Time-domain radiation from large two-dimensional apertures via narrow-waisted gaussian beams," *IEEE Trans. Antennas Propagat.*, vol. 51, pp. 78–88, Jan. 2003.

Vincenzo Galdi (M'98) was born in Salerno, Italy, on July 28, 1970. He received the *Laurea* degree (*summa cum laude*) in electrical engineering and the Ph.D. degree in applied electromagnetics from the University of Salerno, Salerno, Italy, in 1995 and 1999, respectively.

From April to December 1997, he was with the Radio Frequency Division of the European Space Research Technology Centre (ESTEC-ESA), Noordwijk, The Netherlands, where he was involved in developing CAD tools for microwave filters and phased-array antennas with coaxial excitation. In September 1999, he received a European Union Postdoctoral Fellowship through the University of Sannio, Benevento, Italy. From October 1999 to August 2002, he was a Research Associate with the Department of Electrical and Computer Engineering, Boston University, Boston, MA. In September 2002, he joined the Department of Engineering, University of Sannio, Benevento, Italy, where is is currently an Associate Professor of Electromagnetics. His research interests include analytical and numerical techniques for wave propagation in complex environments, path integrals, and stochastic resonance.

Dr. Galdi is the recipient of a 2001 International Union of Radio Science (URSI) "Young Scientist Award." He is a Member of Sigma Xi.

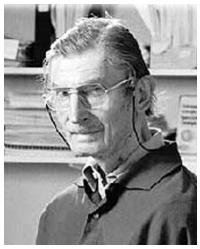

Leopold B. Felsen (S'47–M'54–SM'55–F'62–LF'90) was born in Munich, Germany, on May 7, 1924. He received the B.E.E., M.E.E, and D.E.E. degrees from the Polytechnic Institute of Brooklyn, Brooklyn, NY, in 1948, 1950, and 1952, respectively.

He emigrated to the United States in 1939 and served in the U.S. Army from 1943 to 1946. After graduating from the Polytechnic Institute of Brooklyn (now Polytechnic University) in 1952, he joined the university where he was Dean of Engineering from 1974 to 1978, and then a University Professor in 1978. In 1994, he resigned from the Polytechnic faculty and was granted the status of University Professor Emeritus. He is now Professor of Aerospace and Mechanical Engineering and Professor of Electrical and Computer Engineering at Boston University, Boston, MA (part-time). He is the author or coauthor of over 350 papers and of several books, including the classic *Radiation and Scattering of Waves* (Piscataway, NJ: IEEE Press, 1994). He is an Associate Editor of several professional journals and an Editor of the *Wave Phenomena Series* (New York: Springer-Verlag). His research interests include wave propagation and diffraction in complex environments and in various disciplines, high-frequency asymptotic and short-pulse techniques, and phase-space methods with an emphasis on wave-oriented data processing and imaging.

Dr. Felsen is a Member of Sigma Xi and a Fellow of the Optical Society of America and the Acoustical Society of America. He has held numerous named Visiting Professorships and Fellowships at universities in the United States and abroad, including the Guggenheim in 1973 and the Humboldt Foundation Senior Scientist Award in 1981. In 1974, he was an IEEE/APS (Antennas and Propagation Society) Distinguished Lecturer. He was awarded the Balthasar van der Pol Gold Medal from the International Union of Radio Science (URSI) in 1975, an Honorary Doctorate from the Technical University of Denmark in 1979, the IEEE Heinrich Hertz Gold Medal for 1991, the APS Distinguished Achievement Award for 1998, the IEEE Third Millenium Medal in 2000 (nomination by APS), three Distinguished Faculty Alumnus Awards from Polytechnic University, and an IEEE Centennial Medal in 1984. In 1977 he was elected to the National Academy of Engineering. He served on the APS Administrative Committee from 1963–1966, and as Vice Chairman and Chairman for both the United States (1966–1973) and the International (1978–1984) URSI Commission B.

David A. Castañon (S'68–M'79–SM'98) received the B.S. degree in electrical engineering from Tulane University of Louisiana, New Orleans, LA, in 1971, and the Ph.D. degree in applied mathematics from the Massachusetts Institute of Technology (MIT), Cambridge, MA, in 1976.

From 1976 to 1981, he was a Research Associate with the Laboratory for Information and Decision Systems at MIT. From 1982 to 1990, he was Senior and Chief Research Scientist with Alphatech, Inc., Burlington, MA. Since 1990, he has been a Professor in the Department of Electrical and Computer Engineering, Boston University, Boston, MA. His research interests include stochastic control and estimation, optimization, and image processing.

Dr. Castañon served as a Member of the Board of Governors of the IEEE Control Systems Society. He is also a Member of the AMS, SIAM, and INFORMS.